

Article

Influence of the Inclusion of Off-Nadir Images on UAV-Photogrammetry Projects from Nadir Images and AGL (Above Ground Level) or AMSL (Above Mean Sea Level) Flights

Francisco Agüera-Vega ^{*}, Ezequiel Ferrer-González , Patricio Martínez-Carricondo ,
Julián Sánchez-Hermosilla  and Fernando Carvajal-Ramírez 

Department of Engineering, Research Center for Intensive Mediterranean Agrosystem and Agrifood Biotechnology (CIAIMBITAL), University of Almería, Agrifood Campus of International Excellence, ceiA3, La Cañada de San Urbano, s/n, 04120 Almería, Spain; efg520@inlumine.ual.es (E.F.-G.); pmc824@ual.es (P.M.-C.); jusanche@ual.es (J.S.-H.); carvajal@ual.es (F.C.-R.)

* Correspondence: faguera@ual.es

Abstract: UAV-SfM techniques are in constant development to address the challenges of accurate and precise mapping in terrains with complex morphologies. In contrast with the traditional photogrammetric processes, where only nadir images were considered, the combination of those with oblique imagery, also called off-nadir, has emerged as an optimal solution to achieve higher accuracy in these kinds of landscapes. UAV flights at a constant height above ground level (AGL) have also been considered a possible alternative to improve the resulting 3D point clouds compared to those obtained from constant height above mean sea level (AMSL) flights. The aim of this study is to evaluate the effect of incorporating oblique images as well as the type of flight on the accuracy and precision of the point clouds generated through UAV-SfM workflows for terrains with complex geometries. For that purpose, 58 scenarios with different camera angles and flight patterns for the oblique images were considered, 29 for each type of flight (AMSL and AGL). The 3D point cloud derived from each of the 58 scenarios was compared with a reference 3D point cloud acquired with a terrestrial laser scanner (TLS). The results obtained confirmed that both incorporating oblique images and using AGL flight mode have a positive effect on the mapping. Combination of nadir image blocks, obtained from an AGL crosshatch flight plan, with supplemental oblique images collected with a camera angle of between 20° and 35° yielded the best accuracy and precision records.

Keywords: photogrammetry; SfM; AMSL flights; ASL flights



Citation: Agüera-Vega, F.; Ferrer-González, E.; Martínez-Carricondo, P.; Sánchez-Hermosilla, J.; Carvajal-Ramírez, F. Influence of the Inclusion of Off-Nadir Images on UAV-Photogrammetry Projects from Nadir Images and AGL (Above Ground Level) or AMSL (Above Mean Sea Level) Flights. *Drones* **2024**, *8*, 662. <https://doi.org/10.3390/drones8110662>

Academic Editor: Bo Li

Received: 17 September 2024

Revised: 1 November 2024

Accepted: 5 November 2024

Published: 10 November 2024



Copyright: © 2024 by the authors. Licensee MDPI, Basel, Switzerland. This article is an open access article distributed under the terms and conditions of the Creative Commons Attribution (CC BY) license (<https://creativecommons.org/licenses/by/4.0/>).

1. Introduction

Unmanned aerial vehicles (UAVs) have proven to be instruments capable of providing data with a high level of both spatial and temporal resolution, a very important capability in many different fields of geoscience, such as the study of landslides [1,2], sedimentary geology [3], structural geology [4], engineering [5], mining [6,7], cultural heritage [8], and forest [9]. Compared to conventional airborne and satellite sensors, UAVs are particularly attractive given their lower cost, higher-resolution datasets, and flexibility in image acquisition [10–12]. The miniaturization of sensors, together with the high quality of the data recorded by them, has further increased the versatility of UAVs. In the mapping process, digital cameras are the most commonly used sensors [13,14].

Structure from motion (SfM) paired with multi-view stereopsis (MVS) are the most widely used set of techniques (henceforth UAV-SfM) currently used by software focused on UAV-photogrammetry [15]. The major advances that SfM brought to photogrammetry are that it is able to solve the collinearity equations without support of any ground control point (GCP) [16,17], providing a 3D point cloud in an arbitrary coordinate, as well as a full camera calibration [18,19]. The key points are detected in each image by an algorithm

called a detector and then are identified in different images thanks to matching algorithms that analyze the similarity, consistency, and correspondence of image features [20–22]. The subsequent application of MVS techniques computes a dense 3D point cloud for each pixel in the overlapping area of the images (or for each pixel in the reduced size images) [23].

The main flight parameters to consider for UAV image acquisition are the flight altitude, camera axis angle with regard to the terrain, and frontal (with respect to the flight direction) and side (between flying tracks) overlaps. These parameters, together with sensor dimension, resolution, and focal length, determine both the ground sample distance (GSD) and the accuracy of the photogrammetric projects [13]. Traditional flight plans consist of parallel flight lines at a constant height above mean sea level (AMSL), with pre-fixed frontal and side overlaps, and with the camera axis vertically oriented (nadir angle) [24,25]. These flight plans are not appropriate for collecting images containing features exposed along vertical slope façades. A better approach consists of flight path lines oriented in parallel to the vertical features and camera axis perpendicular to them [26,27]. Nevertheless, in more complex morphology terrains where features of interest (e.g., slope) do not have the same direction throughout, the commented approach may not capture enough detail or geometric information to obtain reliable results [28–30]. Incorporating oblique images, where the camera axis angles are different from nadir, has been proposed as an optimal alternative approach to study terrains with complex morphology or steep slopes [25,27,29,31]. Furthermore, a combination of nadir and oblique images resulted in improved accuracy of UAV photogrammetric projects compared to the use of nadir-only imagery due to better internal calibration of the camera [1,11,32–37].

Regarding the flight altitude, it is well known that in terrains with high elevation range or high relief, imagery from a constant height AMSL often results in a poor image overlap, providing also inconsistent GSD for the surveys. Flights at a constant elevation above ground level (AGL) might help to solve the problem [38,39], contributing to the efficiency of the dense image matching algorithms, which are used to calculate the dense point clouds, and therefore improving the accuracy and precision of the UAV photogrammetric projects [40]. The major drawback of AGL flights is the need to have quality digital elevation models (DEMs) that allow the UAV to follow the non-flat terrain. Despite the fact that DEMs from worldwide and national levels are available, it is recommended to use DEMs generated from previous surveys of the study site in order to avoid problems with the resolution or lack of updating [38,41,42]. The lack of software that supports terrain data for mission planning might also have been a problem in the past, but currently there are some options available. For instance, UgCS-Mapper [43] is a standalone software that can generate a DEM from images obtained in an initial flight with a geotag accuracy of less than 10 m and containing elevation values.

Although several works dealing with adaptive flight height in regard to the terrain can be found in the scientific literature, no further specifics are offered about flight altitudes and their effect on the accuracy of the generated 3D point clouds [44–46]. In [39], AMSL, AGL, and façade flight modes were compared to determine their influence on the accuracy in a long highwall from an open pit mine. Reference [47] provided an overview of airborne mission planning for the currently available platforms and sensors, but the AGL flight mode is only mentioned. Reference [48] studied the optimization of flight routes for DTM reconstruction based on a procedure assuming a constant UAV flight height.

Taking all the facts mentioned above into account, the authors considered it necessary to deepen the knowledge of how some parameters related to the flight planning, such as the type of flight (AMSL or AGL) as well as camera axis angle and flight pattern for capturing supplemental oblique images, can impact the accuracy and detail of the 3D point cloud obtained from the photogrammetric projects derived from the flights.

This paper builds on previous work [40] to quantitatively evaluate the accuracy of different UAV-SfM datasets processed from combinations of nadir image blocks complemented with several oblique image configurations and angles.

2. Materials and Methods

2.1. Study Area

The study area was located in the Tabernas Desert, Almeria, Southeast Spain (Figure 1a). The southwest vertex coordinates of the smaller rectangle covering the study area were $X = 548,760$ and $Y = 4,096,360$, while the northeast vertex coordinates were $X = 548,860$ and $Y = 4,096,500$ (Figure 1b, UTM, Zone 30, European Terrestrial Reference System 89 (ETRS89)). The extension of the area is $14,000 \text{ m}^2$, with elevations varying between 228 and 260 m, which is a range of 32 m. Location and study area shape are shown in Figure 1c. As shown in Figure 1d, the morphology of the area has a wide range of slopes oriented in all directions. The complex morphology and the absence of vegetation were key factors in order to choose this area (Figure 1b₁).

2.2. UAV Data Acquisition and Scenarios

A DJI Phantom 4 Pro quadcopter was used for collecting the images. It is equipped standard with a complementary metal oxide semiconductor (CMOS) sensor of one inch size and 20 megapixels. The camera has a f2.8/f11, 8 mm wide-angle lens with an equivalent focal length of 24 mm in 35 mm format. This UAV was equipped with a Global Navigation Satellite System (GNSS) that records geolocation (x, y, z) to a manufacturer-stated accuracy of $\pm 1.5 \text{ m}$ (horizontal) and $\pm 0.5 \text{ m}$ (vertical). The camera is mounted on a three-axis gimbal that can be adjusted to capture images between 0° (horizontal) and 90° (nadir), with a manufacturer-stated accuracy of $\pm 0.02^\circ$ [49].

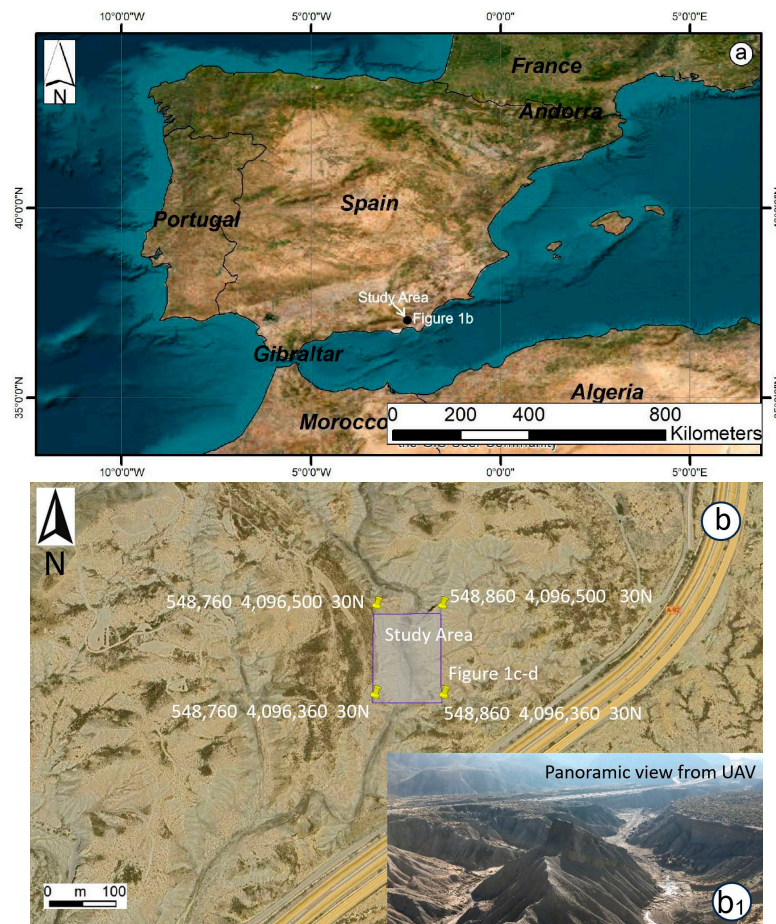


Figure 1. Cont.

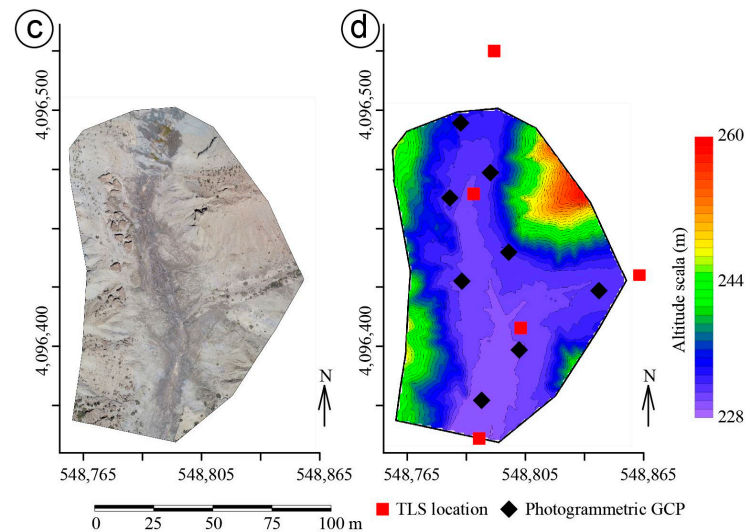


Figure 1. (a) Study area location, marked by a black dot; (b) study area situation, marked by a rectangle with coordinates of its vertices; (b₁) panoramic view, taken from UAV; (c) location and detailed definition of the shape of the study area; (d) scale color contour map, where TLS and ground control points (GCPs) of photogrammetric projects are marked. Coordinates refer to UTM (Zone 30, European Terrestrial Reference System 89 (ETRS89)), (EGM08 geoid model).

To develop the research, the UAV was programmed to follow autonomously a route consisting of several straight lines oriented North–South (N–S), followed by several straight lines oriented East–West (E–W), to obtain a double-grid image block. Frontal overlap was set at 90%, while side overlap was set at 70% for all the flights. These overlap values were chosen on the basis of the results reported by [40]. The camera was fixed with a nadir orientation (90°). To study the effect of varying the distance of the camera to the ground during the course of the flight, two flights were carried out following the designed route, one in AMSL mode and the other one in AGL mode. These two flights were called reference flights. The number of straight lines oriented in N–S were six for AMSL flights and four for AGL flights. On the other hand, the number of straight lines oriented E–W were five for AMSL flight, and three for AGL flight.

Furthermore, to study the influence of supplemental oblique images on the accuracy and precision of photogrammetric project results, five flight paths with different trajectories were programmed and executed in automatic mode (in Figure 2: trajectories a, b, c, e, and f). Each of them was executed four times, each with a different camera angle (11.25°, 22.5°, 33.75°, and 45°), all of them in AMSL mode. Twenty flights were carried out, which were called auxiliary flights.

In the study, the images from some of these were combined, and, finally, the oblique-image patterns evaluated were:

A-CROSS: oblique images formed a cross centered in the study area with one flight path in the NS direction and the other in the EW direction. In each flight path, the consecutive images were facing the opposing direction (Figure 2a).

B-BOX EX: oblique images were arranged in a rectangular box around the study area and pointing towards the interior (Figure 2b).

C-BOX IN: oblique images were arranged in a rectangular box inside the study area and pointing towards the interior (Figure 2c).

D-BOX EX + IN: combination of both interior and exterior rectangular boxes (Figure 2d).

E-CUR NS: oblique images were arranged in arcs on the E and W sides of the study area, so these curves ran from N to S (Figure 2e).

F-CUR EW: oblique images were arranged in arcs on the N and S sides of the study area, so these curves ran from E to W (Figure 2f).

G-CUR NS + EW: combination of both NS and EW curves (Figure 2g).

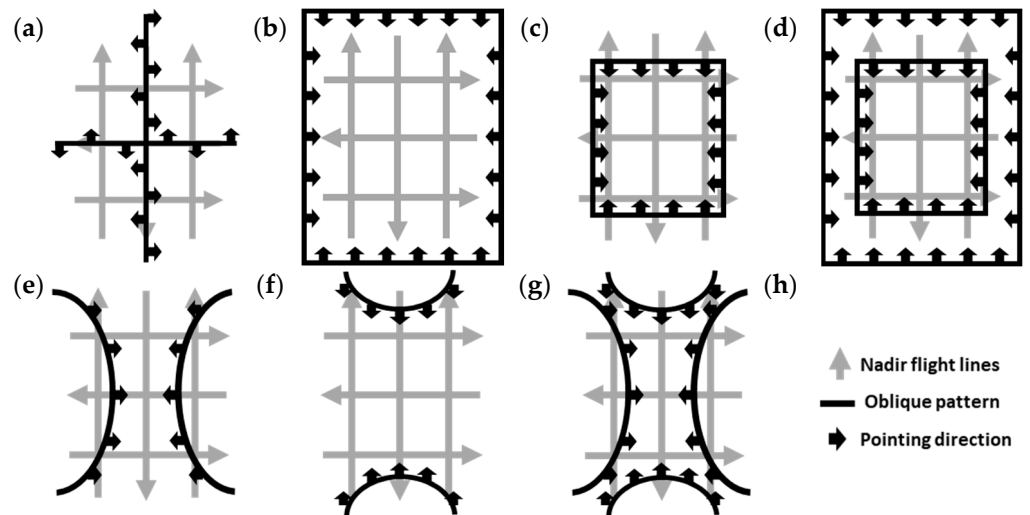


Figure 2. Oblique-image patterns (a) cross-centered in the study area, CROSS; (b) outside box, BOX EX; (c) inside box, BOX IN; (d) outside and inside box, BOX EX + IN; (e) NS curve, CUR NS; (f) EW curve, CUR EW; (g) NS and EW curves, CUR NS + EW; (h) Notes.

Taking into account the two nadir projects (AGL and AMSL) and all the different combinations of camera angles of the oblique-image patterns flight (four angles (11.25°, 22.5°, 33.75°, and 45°), and seven patterns (Figure 2a–g)), a total of 58 different scenarios were studied.

All UAV flights were programmed with UgCS software (Version 4.3.82) [43]. The flight altitude in AMSL mode was set at 65 m above takeoff level, whereas in AGL mode, the flight height was set at 65 m above ground level. Since to plan the AGL flight properly and safely it is necessary to have an updated digital elevation model (DEM), an UAV photogrammetric project was carried out in AMSL mode and a height of 80 m above the takeoff point.

A set of eight ground control points (GCP) were spread over the study area prior to the flights. Since it was impossible to access the higher elevation areas, the GCPs were placed in the lower elevation areas, as shown in Figure 1b. A Trimble R6 rover and base GNSS working in post-processed kinematic (PPK) mode were used to measure the GCPs coordinates. The combination of these measurement instruments and work modes, yields an error of 5 mm + 1 ppm root mean square horizontal and 10 mm + 1 ppm root mean square vertical, as the manufacturer stated.

2.3. Image Processing

The Pix4Dmapper commercial software (V 4.5.6) [50] was used to process the photogrammetric projects. This software integrates an algorithm based on SfM-MVS techniques that provides the dense 3D point cloud for every studied combination.

In order to avoid the influence of possible marking GCP errors on the results, for each reference flight (AMSL and AGL mode), the images were imported, and the eight GCPs were manually marked in every image in which they could be clearly identified. The same was performed for each of the auxiliary flights. Then, for each of the 58 photogrammetric projects studied, the corresponding reference flight and auxiliary flight(s) were combined and processed using the settings shown in Table 1.

For the altitude at which the flights were performed (65 m) and the characteristics of the camera fitted to the UAV, the theoretical GSD was $1.77 \text{ cm} \times \text{pixel}^{-1}$. However, in the AMSL reference flights, there was a variation in the scale in the images due to the terrain geometry, which in turn causes a GSD variation value. The same happened in the auxiliary flights, carried out in AMSL mode, in which the effect of the off-nadir camera orientation on the scale variation was added.

Table 1. Pix4Dmapper processing options selected for all studied scenarios.

Pix4Dmapper Step	Processing Option and Setting
1. Initial project processing	General Keypoint Image Scale: <i>Full</i> Matching Matching Image Pairs: <i>Aerial Grid or Corridor</i> Calibration: Targeted Number of Keypoints: <i>Automatic</i> Calibration Method: <i>Standard. Internal and External</i> Parameters Optimization: <i>All</i> Rematch: <i>Automatic</i>
2. Point cloud and mesh	Point Cloud Image Scale: $\frac{1}{2}$ (<i>Half image size, Default</i>)/ <i>Multiscale</i> Point Density: <i>Optimal</i> Minimum Number of Matches: <i>3</i> Advanced Matching Window Size: 7×7 <i>pixels</i>

Taking into account that the takeoff point elevation for AMSL flights was 230 m and the terrain range elevation varied from 228 m to 260 m, the distance from the UAV to the terrain varied from 35 m, which is equivalent to a GSD value of $0.95 \text{ cm} \times \text{pixel}^{-1}$, to 67 m, which is equivalent to a GSD value of $1.83 \text{ cm} \times \text{pixel}^{-1}$. For the reference flight carried out in AGL mode, this effect was partially eliminated as the camera had a nadir orientation and the distance to the ground during the flight was constant.

2.4. Reference Cloud Acquisition and Processing

The Trimble TX8 (Trimble, Westminster, Colorado, U.S.) terrestrial laser scanner (TLS) was utilized to collect the data to derive a reference 3D point cloud. This model allows the capturing of the coordinates (x, y, z) of one million points per second and has a manufacturer-stated precision of $<0.001 \text{ m}$ at a scanned distance of 80 m and a point spacing of 0.057 m at a scanned distance of 30 m.

Figure 3 shows the workflow chart of this process. In order to completely scan the study area, avoiding as much as possible, gaps and hidden areas, the TLS was placed in five different locations, shown in Figure 1d. Previously, to make possible the georeference of the point clouds generated at each of the TLS locations and merge them into a single cloud covering the whole study area, 18 targets (TLS-GCP) were placed scattered over the terrain, and their coordinates were measured following the same methodology and instruments as previously described for the GCPs.

The process to obtain a single point cloud from the initial five point clouds was divided into three steps. The first step consisted of an initial georeferencing from the location of three TLS-GCPs in each of the clouds. For this purpose, the Trimble Business Center 5.40 commercial software [51] was used. Then, the initially georeferenced clouds were exported in LAS format. In the second step, a fine georeferencing of each cloud was performed considering all TLS-GCPs included in each individual cloud. For this purpose, CloudCompare open source software [52] was used. At this stage, the clouds were merged into one cloud that was already geo-referenced. However, as the 14 TLS-GCPs were not the same as those used to georeference the point clouds generated by the photogrammetric projects, the third step consisted in georeferencing the merged cloud again, using the eight GCPs used for the clouds from the photogrammetric projects. This third step was also carried out using CloudCompare open source software.

Since the merged cloud covered a larger area than the study area, it was clipped, taking into account the contour of the study area. In addition, the merged cloud was filtered to set to 0.002 m, the minimum distance between points. Furthermore, as the clipped cloud consisted of about 180×10^6 points, to avoid excessively long computation times, the final reference cloud was generated by extracting 10% of the points from the clipped cloud.

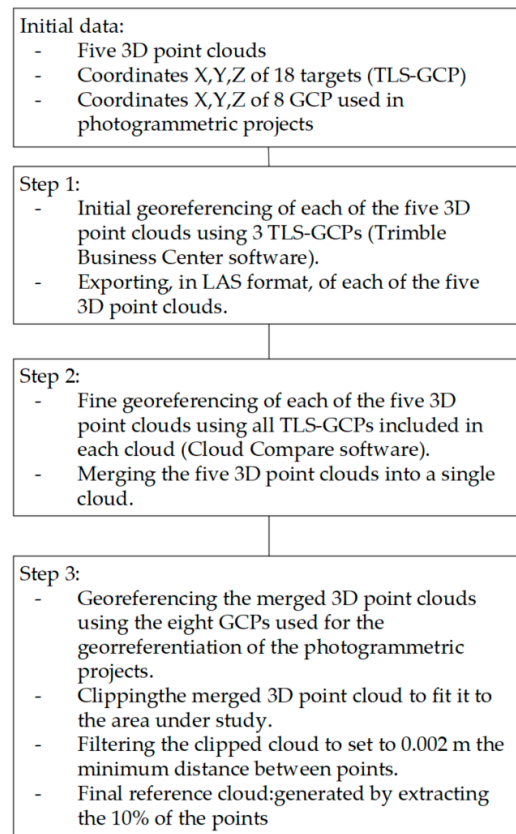


Figure 3. Reference cloud acquisition and processing workflow.

2.5. Accuracy and Precision Assessment

To assess the accuracy and precision of the 3D point clouds derived from the 58 performed photogrammetric projects, the plugin Multiscale Model to Model Cloud Comparison (M3C2) was used, which is included in the CloudCompare software [53]. This algorithm is able to compute the local distances between two point clouds with complex geometry through two steps. Its general description is shown in Figure 4. In the first one, the called normal scale (D) is defined by the user. D represents the diameter of a sphere centered on the point currently studied (j in Figure 4), belonging to the reference cloud. All points of this cloud included in the sphere are used to fit a plane, whose director vector (N in Figure 4) defines the normal orientation of the cloud at that point. In the second step, the user defines a cylinder through the diameter of its base, called the projection scale (d), and its height (h). The cylinder axis contains the director vector calculated in the first step. This cylinder will contain points of reference cloud and points of compared cloud.

The points of each cloud are then projected onto the cylinder axis, and the distance of each projection to the point under study of the reference cloud is calculated. In this way, two sets of values are defined, one corresponding to the reference cloud and another corresponding to the compared cloud. The distance between the mean values (in Figure 4, a_1 for reference cloud and a_2 for compared cloud) derived from each set corresponds to the distance between the clouds at that point. In this work, D was fixed to 0.25 m, d was fixed to 0.15 m, and h was fixed to 1 m. Once the distance between every point of the reference cloud and the compared cloud is calculated, the M3C2 algorithm provides a distribution function of these values, from which the mean and the standard deviation can be calculated. The mean value and the standard deviation value can be assimilated to the accuracy and precision, respectively, of the point clouds derived from each photogrammetric project considered. Since ideally the reference cloud and the compared cloud should be equal, the closer the value of these statistics is to zero, the better the precision and accuracy of the cloud derived from the photogrammetric project.

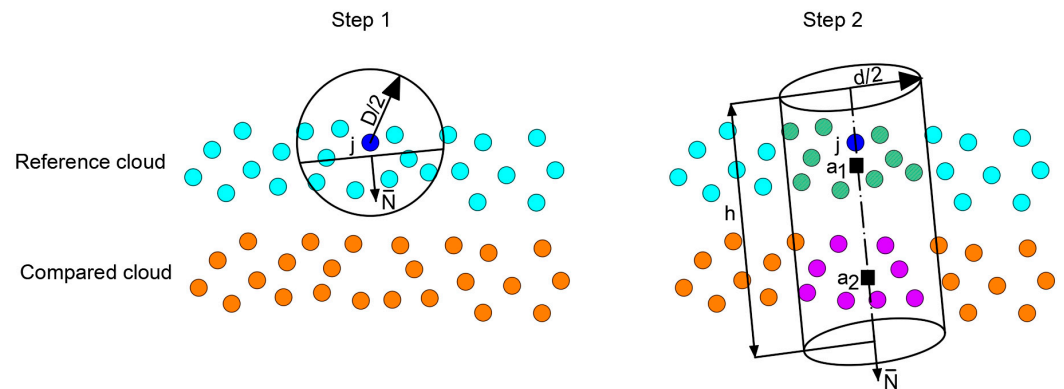


Figure 4. General description of the M3C2 algorithm and the user-defined parameters: D (normal scale), d (projection scale), and h (cylinder height). (**Step 1**): D represents the diameter of a sphere centered on the point currently studied (j). All points of this cloud included in the sphere are used to fit a plane, whose director vector (N) defines the normal orientation of the cloud at that point. (**Step 2**): d and h are defined. The cylinder axis contains the director vector calculated in the first step. The points of each cloud contained in the cylinder (green dots for reference cloud and magenta for compared cloud), are projected onto the cylinder axis, and the distance of each projection to point j is calculated. Two sets of values are defined, one corresponding to the reference cloud and another corresponding to the compared cloud. The distance between the mean values (a_1 and a_2) derived from each set corresponds to the distance between the clouds at that point.

3. Results

Combination of nadir image blocks obtained from a crosshatch flight plan with supplemental oblique images generally resulted in an improvement of both the accuracy and the precision for AMSL and AGL scenarios compared to projects using only nadir images. As can be seen in Figure 5b, only five projects with AGL nadir flights combined with oblique images presented worse accuracy values than the project using only nadir images: BOX EX and CUR EW with image angles of 11.25° , and CROSS, BOX EX, and CUR EW with image angles of 45° . In a direct comparison between AMSL and AGL projects for the different flight patterns and camera angles studied for the oblique images, AGL flights improved both accuracy and precision compared to those from AMSL flights in all cases.

The absolute value of M3C2-calculated mean difference accuracy values achieved for nadir-only image projects were 0.020 m for the AGL flight and 0.035 m for the AMSL flight (Figure 5). The absolute accuracy readings found for projects incorporating oblique images ranged from 0.022 m to 0.035 m for AMSL (Figure 5a) and from 0.006 m to 0.027 m for AGL flights (Figure 5b). AMSL flights achieved the best accuracy readings for camera angles of 22.5° (0.022 m) and 33.75° (0.024 m). Similarly, in the case of AGL flights, the best accuracy values were 0.006 and 0.007 for camera angles of 33.75° and 22.5° , respectively.

In AGL flights (Figure 5b), accuracy generally improved as the camera angle increased from the nadir orientation to camera angles of 22.5° and 33.75° , where the best accuracy values were found independently of the flight pattern followed for capturing the oblique images. Accuracy decreased again for camera angles of 45° for all considered flight patterns. In AMSL flights (Figure 5a), accuracy records improved as the camera angle increased from nadir to 22.5° , except for CROSS and CUR NS flight patterns. The accuracy trended to decrease for camera angles of 33.75° and 45° , except for the BOX EX pattern, where the best accuracy value was found for a camera angle of 33.75° .

With regard to standard deviation distances, or precision (Figure 6), values of 0.106 m and 0.113 m were reached for AGL and AMSL nadir-only projects, respectively, while the precision for datasets incorporating oblique images varied from 0.105 m to 0.111 m for AMSL cases (Figure 6a), and from 0.103 m to 0.106 m for AGL scenarios (Figure 6b). The best precision values were found for camera angles of 22.5° (0.105 m) and 33.75° (0.103 m) for AMSL and AGL flights, respectively. In AGL flights (Figure 6b), the best

precision records were reached for a camera angle of 33.75° in all studied flight patterns, whereas in AMSL flights (Figure 6a) the precision did not show a clear trend. Nevertheless, for most studied flight patterns, five out of seven, the best accuracy was reached for either 22.5° or 33.75°.

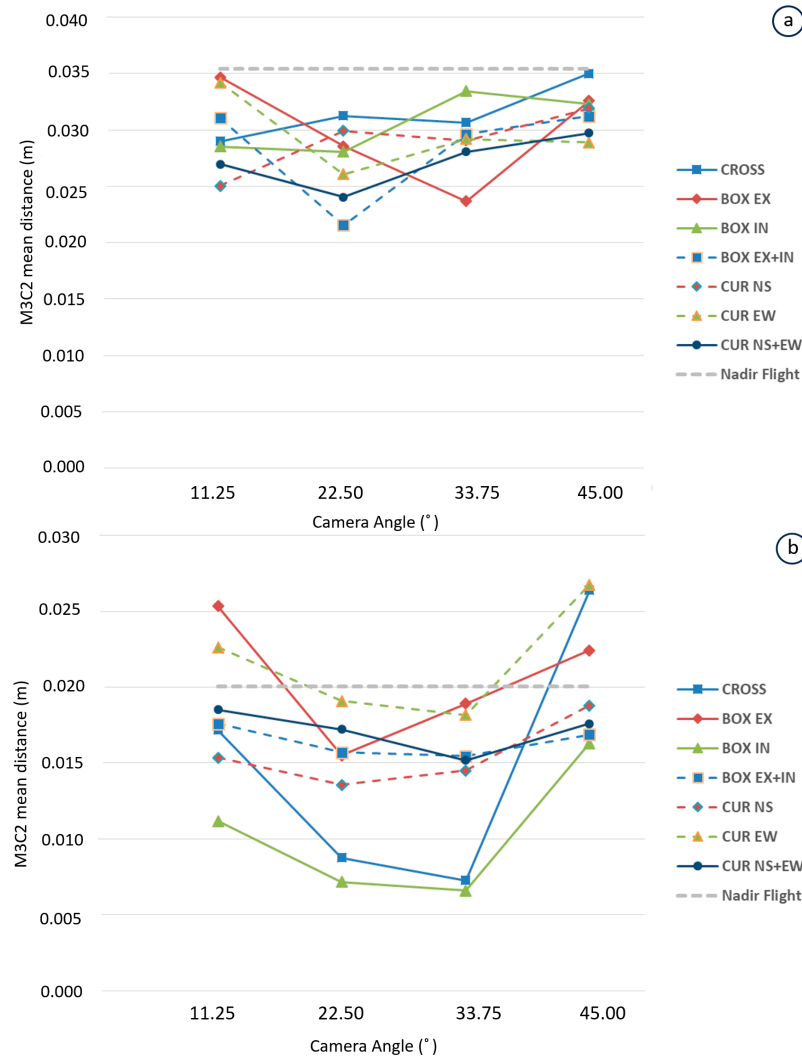


Figure 5. M3C2-calculated mean distance (accuracy) between the TLS reference cloud and clouds obtained from different UAV-SfM image configurations: (a) AMSL; (b) AGL.

As in the case of camera angle, the flight pattern of supplemental oblique images had some effect on the accuracy and precision of the studied combinations. In the case of AGL projects (Figure 5b), accuracy achieved the lowest values for the inner box (BOX IN) flight pattern independently of the camera angle: 0.011, 0.007, 0.006, and 0.017 m for camera angles of 11.25°, 22.5°, 33.75°, and 45°, respectively. For AMSL projects (Figure 5a), results were less consistent, and the lowest accuracy records were reached from different flight patterns depending on the camera angle: CUR NS for 11.25°, BOX EX + IN for 22.5°, BOX EX for 33.75°, and CUR EW for 45°, with accuracy values of 0.025, 0.022, 0.024, and 0.029 m, respectively.

Regarding the precision, the CUR NS + EW flight pattern resulted in the highest precisions for both AMSL (Figure 6a) and AGL (Figure 6b) flights for all camera angles, except for 22.5° in AMSL mode, where the best precision value was reached following an inner/outer box (BOX EX + IN) flight pattern for the supplemental oblique images.

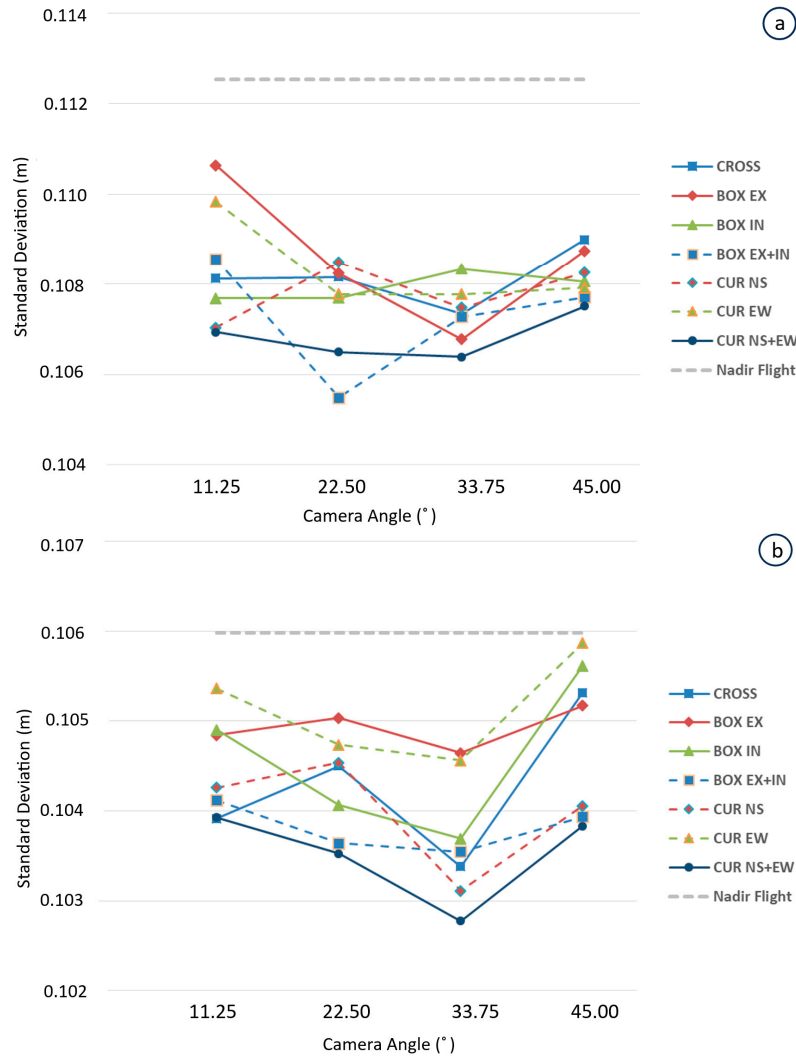


Figure 6. M3C2-calculated standard deviation (precision) between the TLS reference cloud and clouds obtained from different UAV-SfM image configurations: (a) AMSL; (b) AGL.

Figure 7 shows the spatial distribution of the M3C2 distances calculated between the TLS reference cloud and clouds derived from the reference flights (AMSL and AGL), AMSL + CROSS at 22.5° (this cloud presented the best precision and accuracy for all combinations of AMSL and oblique photographs), AGL + BOX IN at 33.75° (this cloud presented the best accuracy for AGL flight combinations), and AGL + CUR NS + CUR EW at 33.75° (this cloud presented the best precision for AGL flight combinations). In this figure, the left column represents the distribution maps of all the points. The middle column represents the distribution of points where distances take positive values, and the right column demonstrates where negative distance has been measured. This figure shows that all the projects depicted have the same pattern of distribution of positive and negative M3C2 distances. Previous works reported a systematic error in the spatial distribution of M3C2 distance [25,54,55], described as the ‘dome effect’. However, Figure 7 shows that both positive and negative M3C2 distances are distributed over the entire study area. Therefore, the ‘dome’ effect does not appear in these projects. For all the projects in Figure 7, the highest positive values were found in the areas with the highest altitude, while the highest absolute negative values were found in the areas with steepest slopes.

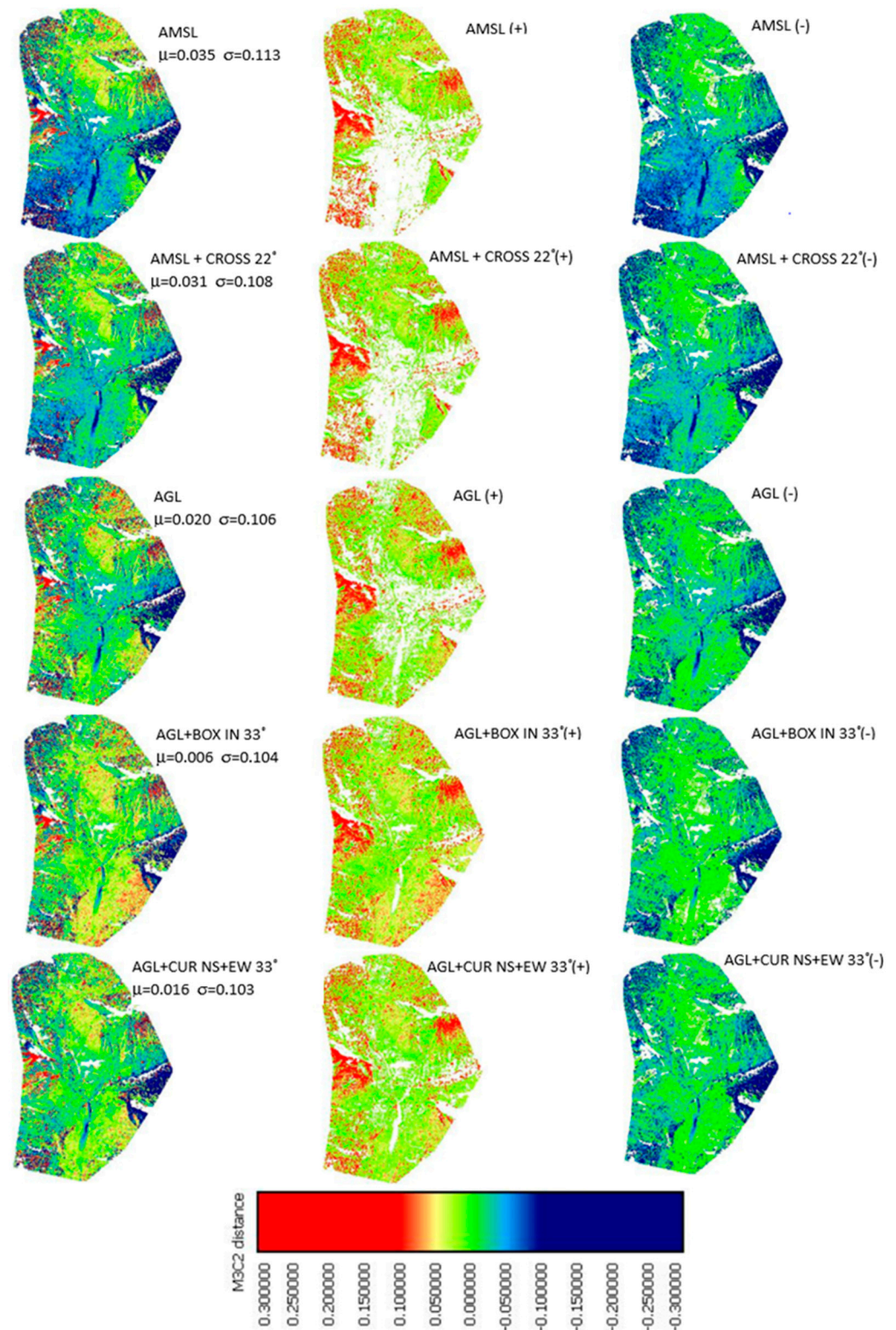


Figure 7. M3C2-calculated distances between TLS reference cloud and clouds obtained from the flights reference (AMSL and AGL), AMSL + CROSS at 22.5° (best accuracy and precision for AMSL and oblique image combinations), AGL + BOX IN at 33.75° (best accuracy for AGL and oblique image combinations), and AGL + CUR NS + CUR EW at 33.75° (best precision for AGL and oblique image combinations). The left column represents the distribution maps of all the points. The middle column represents the distribution of points where distances take positive values, and the right column demonstrates where negative distance has been measured. Dimensions in the color scale are in m.

4. Discussion

Although several studies in the UAV-SfM scientific literature have proposed the combination of nadir and oblique images as an optimal approach to study topographic surfaces with complex morphology, there is yet a need to deepen the knowledge about how certain factors, such as type of flight (AMSL or AGL), camera angle, or flight pattern, might influence the quality and accuracy of the derived 3D point cloud. The aim of this research focused on evaluating the effect of these factors on the accuracy of the dense point clouds yielded by UAV-SfM techniques. With this purpose, 58 scenarios carried out on terrain with a complex morphology were evaluated in order to quantify differences among several oblique imaging configurations in two different types of flights. A highly accurate and georeferenced 3D point cloud generated by TLS was employed as the reference dataset for this assessment. Results shown in this work are based on M3C2 distances, which are calculated in the direction normal to the reference cloud rather than vertical distances.

In line with previous works [25,29,31,38,40], the results obtained in this work indicate that the addition of oblique images into nadir image blocks can be considered an optimal approach to study terrains with complex morphology or steep slopes, improving the spatial accuracy and precision of the 3D point clouds. Furthermore, results show that independently of the camera angle and flight pattern used to collect the supplemental oblique images, AGL projects yield better values than the AMSL projects, which is in agreement with [38], who suggested that in steep terrains the UAV should follow the terrain at a certain height AGL in order to obtain the optimal accuracy. However, since in AMSL projects both the accuracy and precision improve when oblique images are included, regardless of the camera angle and flight pattern of those, this type of flight can be considered an optimal solution when a quality digital elevation model of the study area is not available, since this is necessary to carry out AGL flights.

In [25], UAV-SfM models derived from combination datasets consisting of nadir image blocks supplemented with oblique images from 5° to 35° collected in a high-relief landscape were assessed in AMSL mode. The results suggest that supplemental oblique images obtained with camera angles between 10° and 15° yielded the best accuracy, whereas with camera angles between 25° and 35°, best the precision values were reached. Reference [25] concluded that oblique camera angles between 20° and 35°, increased precision and accuracy by nearly 50% relative to nadir-only image blocks. In the present work, the best precision and accuracy records for AMSL flights were found for either 22.5° or 33.75° camera angles. These angles represent almost the extremes of the range of angles where [25] found the best precision and accuracy. For AGL flights, similar camera angles are strongly recommended considering that, for some flight patterns, camera angles of 11.25° and 45° yielded even worse accuracy than the project using only nadir images. In [56], the impact of the imaging angle on the quality of a 3D coastal cliff face reconstruction was assessed. The accuracy of the reconstruction was very similar for camera angles of 20°, 30°, and 40°, showing a substantial improvement compared to the accuracy of the reconstruction from nadir images. Reference [57] compared the accuracy of photogrammetric projects from nadir only datasets with the accuracy of projects obtained from combinations consisting of the nadir datasets and supplemental oblique images collected with camera angles of 15° and 30°. Both combinations performed better than the nadir project, obtaining the best accuracy values for the project with 30° oblique images.

Regarding the flight pattern used to collect the oblique images, reference [25] found that flight patterns consisting of more images produced datasets with the highest precision but the lowest accuracy. These findings are partially in line with the ones achieved in this work, where the CUR NS + EW and BOX EX + IN flight patterns, which include more images than the others, yielded the best precision for all camera angles studied in both AMSL and AGL flight modes and the best accuracy record for a camera angle of 22.5° in AMSL. Furthermore, the CUR NS + EW flight pattern provided the second-best accuracy for all camera angles in AMSL flight. In the case of AGL flights, which were not considered in [25], BOX IN and CROSS yielded the best accuracy values.

As previously discussed, AGL flights substantially improved the accuracy and precision of the point clouds compared to AMSL flights for all camera angles (0° , 11.25° , 22.5° , 33.75° , and 45°) and flight patterns considered in this research. These findings are in agreement with [39], which carried out research in a long highwall from an open pit mine, where the results reported that AGL flight improved the accuracy over AMSL flight in the proposed scenarios, nadir, and 40° camera angle projects. However, the results obtained in the present work show that the combination of imagery collected with an angle between 20° and 35° and a nadir image block from an AGL flight mode is the optimal combination in order to achieve the best accuracy and precision records, which is similar to the conclusion reached in [40] and contrary to the camera angle of 40° proposed by [39].

5. Conclusions

UAV surveys in terrains with complex morphology or steep slopes are more difficult to carry out than those on flat surfaces, requiring careful planning when capturing the image sets. As suggested by several authors, the results shown in this research confirm that the combination of nadir image blocks with oblique images substantially improves the accuracy and precision of the 3D point clouds obtained from UAV-SfM workflows. Furthermore, the performed study demonstrates that in topographically complex scenes, it is suitable to plan an AGL flight mode, where the UAV follows the terrain at a constant height above the ground.

In high-relief terrain, based on the results from 58 scenarios with different configurations for the oblique images and considering the AMSL and AGL types of flights, combination datasets consisting of a nadir image block collected in AGL flight mode and supplemented with oblique images from camera angles between 20° and 35° are the optimal approach in order to achieve the best accuracy and precision. Regarding the flight pattern for capturing oblique images, the results do not show an optimal pattern that covers all the scenarios.

AGL flights require a DEM with a suitable resolution and topographical accuracy of the study area. In case the digital elevation models available have an inadequate resolution and/or accuracy, these can be easily generated from a set of images containing georeferencing data in their EXIF data. Nevertheless, results from this research showed that in AMSL projects both accuracy and precision improved when oblique images were included, allowing this type of flight to be considered an alternative approach when a quality DEM is not available or cannot be generated.

Author Contributions: Conceptualization, F.A.-V. and E.F.-G.; methodology, F.A.-V., P.M.-C., and F.C.-R.; software, P.M.-C. and J.S.-H.; validation, F.A.-V., and F.C.-R.; formal analysis, F.A.-V.; E.F.-G., and P.M.-C.; resources, F.A.-V.; data curation, F.A.-V., E.F.-G.; P.M.-C., F.C.-R., and J.S.-H.; writing—original draft preparation, F.A.-V. and E.F.-G.; rating—review and editing, F.A.-V. All authors have read and agreed to the published version of the manuscript.

Funding: This research was funded by University of Almería (Spain) and by FEDER funds of the European Union (PPUENTE2021/003).

Data Availability Statement: The original data created in the study are openly available in Mendeley Data at DOI: 10.17632/mvd5c3mc3v.1.

Acknowledgments: The authors would like to thank Delegación Territorial de Desarrollo Sostenible en Almería (Consejería de Agricultura, Ganadería, Pesca y Desarrollo Sostenible, Junta de Andalucía) for continued research access to the Paraje Natural Desierto de Tabernas.

Conflicts of Interest: The authors declare no conflict of interest.

References

1. Sun, J.; Yuan, G.; Song, L.; Zhang, H. Unmanned Aerial Vehicles (UAVs) in Landslide Investigation and Monitoring: A Review. *Drones* **2024**, *8*, 30. [\[CrossRef\]](#)
2. Fernández, T.; Pérez, J.; Cardenal, J.; Gómez, J.; Colomo, C.; Delgado, J. Analysis of Landslide Evolution Affecting Olive Groves Using UAV and Photogrammetric Techniques. *Remote Sens.* **2016**, *8*, 837. [\[CrossRef\]](#)
3. Chesley, J.T.; Leier, A.L.; White, S.; Torres, R. Using unmanned aerial vehicles and structure-from-motion photogrammetry to characterize sedimentary outcrops: An example from the Morrison Formation, Utah, USA. *Sediment. Geol.* **2017**, *354*, 1–8. [\[CrossRef\]](#)
4. Bemis, S.P.; Micklethwaite, S.; Turner, D.; James, M.R.; Akciz, S.; Thiele, S.T.; Bangash, H.A. Ground-based and UAV-Based photogrammetry: A multi-scale, high-resolution mapping tool for structural geology and paleoseismology. *J. Struct. Geol.* **2014**, *69*, 163–178. [\[CrossRef\]](#)
5. Zulkipli, M.A.; Tahar, K.N. Multirotor UAV-Based Photogrammetric Mapping for Road Design. *Int. J. Opt.* **2018**, *2018*, 1871058. [\[CrossRef\]](#)
6. Campbell, S.; Simmons, R.; Rickson, J.; Waine, T.; Simms, D. Using Near-Surface Photogrammetry Assessment of Surface Roughness (NSPAS) to assess the effectiveness of erosion control treatments applied to slope forming materials from a mine site in West Africa. *Geomorphology* **2018**, *322*, 188–195. [\[CrossRef\]](#)
7. Gong, C.; Lei, S.; Bian, Z.; Liu, Y.; Zhang, Z.; Cheng, W. Analysis of the Development of an Erosion Gully in an Open-Pit Coal Mine Dump During a Winter Freeze-Thaw Cycle by Using Low-Cost UAVs. *Remote Sens.* **2019**, *11*, 1356. [\[CrossRef\]](#)
8. Martínez-Carricondo, P.; Carvajal-Ramírez, F.; Yero-Paneque, L.; Agüera-Vega, F. Combination of HBIM and UAV photogrammetry for modelling and documentation of forgotten heritage. Case study: Isabel II dam in Níjar (Almería, Spain). *Herit. Sci.* **2021**, *9*, 95. [\[CrossRef\]](#)
9. Carvajal-Ramírez, F.; da Silva, J.R.M.; Agüera-Vega, F.; Martínez-Carricondo, P.; Serrano, J.; Moral, F.J. Evaluation of fire severity indices based on pre- and post-fire multispectral imagery sensed from UAV. *Remote Sens.* **2019**, *11*, 993. [\[CrossRef\]](#)
10. Colomina, I.; Molina, P. Unmanned aerial systems for photogrammetry and remote sensing: A review. *ISPRS J. Photogramm. Remote Sens.* **2014**, *92*, 79–97. [\[CrossRef\]](#)
11. James, M.R.; Robson, S.; d’Oleire-Oltmanns, S.; Niethammer, U. Optimising UAV topographic surveys processed with structure-from-motion: Ground control quality, quantity and bundle adjustment. *Geomorphology* **2017**, *280*, 51–66. [\[CrossRef\]](#)
12. Hugenholtz, C.H.; Whitehead, K.; Brown, O.W.; Barchyn, T.E.; Moorman, B.J.; LeClair, A.; Riddell, K.; Hamilton, T. Geomorphological mapping with a small unmanned aircraft system (sUAS): Feature detection and accuracy assessment of a photogrammetrically-derived digital terrain model. *Geomorphology* **2013**, *194*, 16–24. [\[CrossRef\]](#)
13. Manconi, A.; Ziegler, M.; Blöchliger, T.; Wolter, A. Technical note: Optimization of unmanned aerial vehicles flight planning in steep terrains. *Int. J. Remote Sens.* **2019**, *40*, 2483–2492. [\[CrossRef\]](#)
14. Toth, C.; Józków, G. Remote sensing platforms and sensors: A survey. *ISPRS J. Photogramm. Remote Sens.* **2016**, *115*, 22–36. [\[CrossRef\]](#)
15. Westoby, M.J.; Brasington, J.; Glasser, N.F.; Hambrey, M.J.; Reynolds, J.M. “Structure-from-Motion” photogrammetry: A low-cost, effective tool for geoscience applications. *Geomorphology* **2012**, *179*, 300–314. [\[CrossRef\]](#)
16. Cirillo, D.; Cerritelli, F.; Agostini, S.; Bello, S.; Lavecchia, G.; Brozzetti, F. Integrating Post-Processing Kinematic (PPK)–Structure-from-Motion (SfM) with Unmanned Aerial Vehicle (UAV) Photogrammetry and Digital Field Mapping for Structural Geological Analysis. *ISPRS Int. J. Geo-Inf.* **2022**, *11*, 437. [\[CrossRef\]](#)
17. Famiglietti, N.A.; Cecere, G.; Grasso, C.; Memmolo, A.; Vicari, A. A test on the potential of a low cost unmanned aerial vehicle rtk/ppk solution for precision positioning. *Sensors* **2021**, *21*, 3882. [\[CrossRef\]](#)
18. Fonstad, M.A.; Dietrich, J.T.; Courville, B.C.; Jensen, J.L.; Carbonneau, P.E. Topographic structure from motion: A new development in photogrammetric measurement. *Earth Surf. Process. Landforms* **2013**, *38*, 421–430. [\[CrossRef\]](#)
19. Pérez, M.; Agüera, F.; Carvajal, F. Digital Camera Calibration Using Images Taken From an Unmanned Aerial Vehicle. *Int. Arch. Photogramm. Remote Sens. Spat. Inf. Sci.* **2012**, XXXVIII-1/C22, 167–171. [\[CrossRef\]](#)
20. Ao, T.; Liu, X.; Ren, Y.; Luo, R.; Xi, J. An approach to scene matching algorithm for UAV autonomous navigation. In Proceedings of the 2018 Chinese Control And Decision Conference (CCDC), Shenyang, China, 9–11 June 2018; pp. 996–1001. [\[CrossRef\]](#)
21. Mousavi, V.; Varshosaz, M.; Remondino, F. Using information content to select keypoints for uav image matching. *Remote Sens.* **2021**, *13*, 1302. [\[CrossRef\]](#)
22. Liu, C.; Xu, J.; Wang, F. A Review of Keypoints’ Detection and Feature Description in Image Registration. *Sci. Program.* **2021**, *2021*, 8509164. [\[CrossRef\]](#)
23. Furukawa, Y.; Ponce, J. Accurate, dense, and robust multi-view stereopsis. In Proceedings of the IEEE Computer Society Conference on Computer Vision and Pattern Recognition, Minneapolis, MN, USA, 17–22 June 2007.
24. Martín, R.A.; Rojas, I.; Franke, K.; Hedengren, J.D. Evolutionary view planning for optimized UAV terrain modeling in a simulated environment. *Remote Sens.* **2016**, *8*, 26–50. [\[CrossRef\]](#)
25. Nesbit, P.R.; Hugenholtz, C.H. Enhancing UAV-SfM 3D model accuracy in high-relief landscapes by incorporating oblique images. *Remote Sens.* **2019**, *11*, 239. [\[CrossRef\]](#)
26. Martínez-Carricondo, P.; Agüera-Vega, F.; Carvajal-Ramírez, F. Use of UAV-photogrammetry for Quasi-vertical wall surveying. *Remote Sens.* **2020**, *12*, 2221. [\[CrossRef\]](#)

27. Agüera-Vega, F.; Carvajal-Ramírez, F.; Martínez-Carricondo, P.; Sánchez-Hermosilla López, J.; Mesas-Carrascosa, F.J.; García-Ferrer, A.; Pérez-Porras, F.J. Reconstruction of extreme topography from UAV structure from motion photogrammetry. *Meas. J. Int. Meas. Confed.* **2018**, *121*, 127–138. [CrossRef]
28. Pavlis, T.L.; Mason, K.A. The new world of 3D geologic mapping. *GSA Today* **2017**, *27*, 4–10. [CrossRef]
29. Rossi, P.; Mancini, F.; Dubbini, M.; Mazzone, F.; Capra, A. Combining nadir and oblique uav imagery to reconstruct quarry topography: Methodology and feasibility analysis. *Eur. J. Remote Sens.* **2017**, *50*, 211–221. [CrossRef]
30. Vollgger, S.A.; Cruden, A.R. Mapping folds and fractures in basement and cover rocks using UAV photogrammetry, Cape Liptrap and Cape Paterson, Victoria, Australia. *J. Struct. Geol.* **2016**, *85*, 168–187. [CrossRef]
31. Tu, Y.H.; Johansen, K.; Aragon, B.; Stutsel, B.M.; Angel, Y.; Lopez Camargo, O.A.L.; Al-Mashharawi, S.K.M.; Jiang, J.; Ziliani, M.G.; McCabe, M.F. Combining Nadir, Oblique, and Façade Imagery Enhances Reconstruction of Rock Formations Using Unmanned Aerial Vehicles. *IEEE Trans. Geosci. Remote Sens.* **2021**, *59*, 9987–9999. [CrossRef]
32. Harwin, S.; Lucieer, A.; Osborn, J. The impact of the calibration method on the accuracy of point clouds derived using unmanned aerial vehicle multi-view stereopsis. *Remote Sens.* **2015**, *7*, 11933–11953. [CrossRef]
33. Carbonneau, P.E.; Dietrich, J.T. Cost-effective non-metric photogrammetry from consumer-grade sUAS: Implications for direct georeferencing of structure from motion photogrammetry. *Earth Surf. Process. Landforms* **2017**, *42*, 473–486. [CrossRef]
34. Gerke, M.; Nex, F.; Remondino, F.; Jacobsen, K.; Kremer, J.; Karel, W.; Huf, H.; Ostrowski, W. Orientation of oblique airborne image sets—Experiences from the ISPRS/EuroSDR benchmark on multi-platform photogrammetry. *Int. Arch. Photogramm. Remote Sens. Spat. Inf. Sci.—ISPRS Arch.* **2016**, *2016*, 185–191. [CrossRef]
35. Jiang, S.; Jiang, W. Efficient SfM for oblique UAV images: From match pair selection to geometrical verification. *Remote Sens.* **2018**, *10*, 1246. [CrossRef]
36. Verykokou, S.; Ioannidis, C. Exterior orientation estimation of oblique aerial images using SfM-based robust bundle adjustment. *Int. J. Remote Sens.* **2020**, *41*, 7217–7254. [CrossRef]
37. Nex, F.; Gerke, M.; Remondino, F.; Przybilla, H.J.; Baumker, M.; Zurhorst, A. Isprs benchmark for multi-platform photogrammetry. *ISPRS Ann. Photogramm. Remote Sens. Spat. Inf. Sci.* **2015**, *2*, 135–142. [CrossRef]
38. Trajkovski, K.K.; Grigillo, D.; Petrovič, D. Optimization of UAV flight missions in steep terrain. *Remote Sens.* **2020**, *12*, 1293. [CrossRef]
39. Zapico, I.; Laronne, J.B.; Castillo, L.S.; Martín Duque, J.F. Improvement of workflow for topographic surveys in long highwalls of open pit mines with an unmanned aerial vehicle and structure from motion. *Remote Sens.* **2021**, *13*, 3353. [CrossRef]
40. Agüera-Vega, F.; Ferrer-González, E.; Carvajal-Ramírez, F.; Martínez-Carricondo, P.; Rossi, P.; Mancini, F. Influence of AGL flight and off-nadir images on UAV-SfM accuracy in complex morphology terrains. *Geocarto Int.* **2022**, *37*, 12892–12912. [CrossRef]
41. Manfreda, S.; Dvorak, P.; Mullerova, J.; Herban, S.; Vuono, P.; Justel, J.J.A.; Perks, M. Assessing the accuracy of digital surface models derived from optical imagery acquired with unmanned aerial systems. *Drones* **2019**, *3*, 15. [CrossRef]
42. Jiménez-Jiménez, S.I.; Ojeda-Bustamante, W.; Marcial-Pablo, M.D.J.; Enciso, J. Digital terrain models generated with low-cost UAV photogrammetry: Methodology and accuracy. *ISPRS Int. J. Geo-Inf.* **2021**, *10*, 285. [CrossRef]
43. Mapper UgCS Software (Version 4.3.82). 2022. Available online: <https://www.sphengineering.com/flight-planning/ugcs-mapper> (accessed on 1 October 2024).
44. Cook, K.L. An evaluation of the effectiveness of low-cost UAVs and structure from motion for geomorphic change detection. *Geomorphology* **2017**, *278*, 195–208. [CrossRef]
45. Rossini, M.; Di Mauro, B.; Garzonio, R.; Baccolo, G.; Cavallini, G.; Mattavelli, M.; De Amicis, M.; Colombo, R. Rapid melting dynamics of an alpine glacier with repeated UAV photogrammetry. *Geomorphology* **2018**, *304*, 159–172. [CrossRef]
46. Valkaniotis, S.; Papathanassiou, G.; Ganas, A. Mapping an earthquake-induced landslide based on UAV imagery; case study of the 2015 Okeanos landslide, Lefkada, Greece. *Eng. Geol.* **2018**, *245*, 141–152. [CrossRef]
47. Pepe, M.; Fregonese, L.; Scaioni, M. Planning airborne photogrammetry and remote-sensing missions with modern platforms and sensors. *Eur. J. Remote Sens.* **2018**, *51*, 412–435. [CrossRef]
48. Yang, C.H.; Tsai, M.H.; Kang, S.C.; Hung, C.Y. UAV path planning method for digital terrain model reconstruction—A debris fan example. *Autom. Constr.* **2018**, *93*, 214–230. [CrossRef]
49. Dji.com dji.com. Available online: <https://www.dji.com> (accessed on 1 October 2024).
50. Pix4Dmapper (Version 4.6.4). Available online: <https://www.pix4d.com/product/pix4dmapper-photogrammetry-software> (accessed on 20 September 2024).
51. Trimble. Available online: <https://geospatial.trimble.com/en/products/software/trimble-business-center> (accessed on 1 October 2024).
52. CloudCompare (Version 2.10.3) [GPL Software]. Available online: <http://www.cloudcompare.org> (accessed on 1 October 2024).
53. Lague, D.; Brodu, N.; Leroux, J. Accurate 3D comparison of complex topography with terrestrial laser scanner: Application to the Rangitikei canyon (N-Z). *ISPRS J. Photogramm. Remote Sens.* **2013**, *82*, 10–26. [CrossRef]
54. James, M.R.; Robson, S. Mitigating systematic error in topographic models derived from UAV and ground-based image networks. *Earth Surf. Process. Landforms* **2014**, *39*, 1413–1420. [CrossRef]
55. James, M.R.; Antoniazza, G.; Robson, S.; Lane, S.N. Mitigating systematic error in topographic models for geomorphic change detection: Accuracy, precision and considerations beyond off-nadir imagery. *Earth Surf. Process. Landforms* **2020**, *45*, 2251–2271. [CrossRef]

-
56. Jaud, M.; Letortu, P.; Théry, C.; Grandjean, P.; Costa, S.; Maquaire, O.; Davidson, R.; Le Dantec, N. UAV survey of a coastal cliff face—Selection of the best imaging angle. *Meas. J. Int. Meas. Confed.* **2019**, *139*, 10–20. [[CrossRef](#)]
 57. Štroner, M.; Urban, R.; Seidl, J.; Reindl, T.; Brouček, J. Photogrammetry using UAV-mounted GNSS RTK: Georeferencing strategies without GCPs. *Remote Sens.* **2021**, *13*, 1336. [[CrossRef](#)]

Disclaimer/Publisher’s Note: The statements, opinions and data contained in all publications are solely those of the individual author(s) and contributor(s) and not of MDPI and/or the editor(s). MDPI and/or the editor(s) disclaim responsibility for any injury to people or property resulting from any ideas, methods, instructions or products referred to in the content.